INTERNATIONAL JOURNAL FOR NUMERICAL METHODS IN FLUIDS
Int. J. Numer. Meth. Fluids 2009; **59**:1011–1033
Published online 9 July 2008 in Wiley InterScience (www.interscience.wiley.com). DOI: 10.1002/fld.1848

A robust algorithm for computing fluid flows on highly non-smooth staggered grids

A. Rabiee[1,*,†], A. N. Ziaei[2,‡], M. M. Alishahi[1,§] and H. Emdad[1,‡]

[1]*Department of Mechanical Engineering, Shiraz University, Shiraz, Iran*
[2]*Department of Water Engineering, Shiraz University, Shiraz, Iran*

SUMMARY

A new method for computing the fluid flow in complex geometries using highly non-smooth and non-orthogonal staggered grid is presented. In a context of the SIMPLE algorithm, pressure and physical tangential velocity components are used as dependent variables in momentum equations. To reduce the sensitivity of the curvature terms in response to coordinate line orientation change, these terms are exclusively computed using Cartesian velocity components in momentum equations. The method is then used to solve some fairly complicated 2-D and 3-D flow field using highly non-smooth grids. The accuracy of results on rough grids (with sharp grid line orientation change and non-uniformity) was found to be high and the agreement with previous experimental and numerical results was quite good. Copyright © 2008 John Wiley & Sons, Ltd.

Received 7 January 2008; Revised 25 March 2008; Accepted 15 April 2008

KEY WORDS: staggered grid; non-smooth; non-uniform; SIMPLE; non-orthogonal; curvilinear coordinate

1. INTRODUCTION

The requirement to model complicated flow fields has generated a growing interest in the development of boundary conforming numerical techniques capable of handling grid non-uniformity and non-smoothness. For this purpose, finite volume besides to other methods has been continuously modified and enhanced. Experience has shown that solving the flow field using structured grids is more accurate than unstructured grids especially near solid boundaries [1]. However, structured grid in a complex geometry brings about non-smoothness and non-uniformity that should be taken care of by the numerical technique robustness.

*Correspondence to: A. Rabiee, Department of Mechanical Engineering, Shiraz University, Shiraz, Iran.
†E-mail: rabiee@shirazu.ac.ir
‡Assistant Professor.
§Professor.

Several methods have been proposed for solving the incompressible Navier–Stokes (NS) equations in arbitrary domains with orthogonal and non-orthogonal structured grids. These methods differ in dependent variables used in the momentum equations and the choice of grid layout (staggered and non-staggered).

Owing to a number of difficulties in non-staggered schemes [2], some researchers such as Ikohagi *et al*. [3], Koshizuka *et al*. [4], and Wesseling *et al*. [5] have sought to extend the staggered scheme from Cartesian to general curvilinear coordinates.

Wesseling *et al*. [6] showed that the staggered scheme can be generalized from Cartesian to general coordinates while maintaining accuracy even on a very non-uniform grid. In this manner, the use of non-orthogonal curvilinear grids brings about more flexibility with regard to concentration of grid points in the desired regions. Therefore, the numerical methods that are capable of producing suitable results in highly non-smooth grids are much desirable. On the other hand, the use of non-orthogonal curvilinear coordinate systems can generate a number of difficulties. Calculations of the metric quantities are usually based on grid discrete points rather than the analytical functions of transformation. This may lead to significant numerical errors or even unrealistic solutions, especially for non-smooth grids [7]. The computation of cross-derivatives terms in non-orthogonal grids may cause significant deterioration of the convergence rate of some common solution procedures [8]. Hence, different approaches have been proposed to deal with these non-orthogonal terms (see [9–13]).

He and Salcudean [14] proposed a method to compute fluid flows in complex geometries using a body-fitted non-orthogonal grid. They used a second-order accurate numerical scheme to describe the cross-derivative terms. This method is desirable for non-orthogonal and moderately non-smooth grids. However, the use of highly non-smooth grids in the context of this method should be avoided in order to keep reasonable accuracy. They pointed out that the way of dealing with the curvature terms should be modified for highly non-smooth grids. This method has been used by a couple of researchers to simulate fairly complicated flow fields (e.g. Ziaei *et al.* [15] and Nikseresh *et al*. [16]). He *et al*. [17] presented a multi-grid method to model the flow field in complex 3-D geometries using non-orthogonal curvilinear grids. They also tried to eliminate the deficiencies of the He and Salcudean [14] method in the areas of inferior grids.

Wesseling *et al*. [5, 6] proposed accurate metrics calculation in order to eliminate the non-smooth grid difficulties. Loudyi *et al.* [18] presented an improved least-squares gradient technique to consider the non-orthogonality. Rüaak *et al.* [19] used a method based on tensor analysis to transform the equations from curvilinear into rectangular grids; thus, a modified formulation of the differential equations is applied.

It is noteworthy that in addition to staggered and non-staggered methods, other numerical tools are also used to solve the NS equations in complex geometries. Among them mesh less (e.g. Monaghan *et al*. [20]) and immersed boundary [21] methods can be mentioned.

This research is a part of activities targeted toward the production of a 3-D robust computational fluid dynamics (CFD) code to investigate two-phase free-surface flows. Therefore, the main objective of this study is to test and verify the capabilities of the main solver in dealing with non-smooth grids. In the present study, a new straightforward method based on He and Salcudean [14] is introduced that improves the capability of the former method in solving the flow field problems including highly non-uniform and non-smooth grids and rapid changes in the direction of coordinate lines. The pressure and tangential (non-Cartesian) velocity components are used as the dependent variables in the momentum equations. The SIMPLE algorithm [22] is used for velocity–pressure coupling. However, due to high sensitivity of results to coordinate line direction

DOI: 10.1002/fld

changes, it is shown that the curvature terms in the momentum equations should not be merely determined by simple interpolation or extrapolation of the tangential velocities. Therefore, as the main contribution of the present study, curvature terms are calculated using Cartesian velocity components. These components are carefully computed from dependent velocity components and relevant contravariant base vectors.

In the rest of this paper, the original method is briefly described and its shortcomings in highly non-smooth grids will be highlighted. After that, the required modification is explained in detail. The modified method will then be implemented to solve some fairly complicated 2-D and 3-D flow fields using highly non-smooth grids. The present numerical results will be compared with previous numerical and experimental results. Finally, the method will be used to solve a 2-D turbulent duct flow using high-Reynolds k–ε model on a non-smooth grid.

2. FORMULATION AND NUMERICAL PROCEDURE

The governing equations are the NS equations for incompressible viscous fluids. This section describes a modified algorithm based on He and Salcudean [14] for discretization of a generalized transport equation that is capable of handling highly non-uniform, non-orthogonal grids. Discretization of NS equations will be described later in this section.

2.1. Finite volume discretization of equations in curvilinear coordinates

The proposed algorithm is a finite volume method implemented in general curvilinear coordinates. To illustrate the procedure, consider the following generalized transport equation:

$$\frac{\partial(\rho\phi)}{\partial t}+\nabla\cdot(\rho\mathbf{u}\phi)-\nabla\cdot(\Gamma\nabla\phi)+C(\phi)=0 \tag{1}$$

where the dependent variable is denoted by ϕ and $\mathbf{u}$, ρ, Γ, and C are velocity vector, density, diffusion coefficient, and source term, respectively. The second and third terms in (1) represent transport of ϕ by convection and the molecular diffusion.

In the present algorithm, physical tangential velocity components are used as dependent variables in the momentum equations. These are contravariant velocity components normalized in an appropriate manner. The geometric quantities of cells are directly computed on a uniform grid with a mesh size $\Delta\xi_i=1$ in computational domain. These geometric quantities are illustrated in Figure 1. The unit tangent vectors $\mathbf{e}_i$ $(i=1,2,3)$ or covariant base vectors that are locally parallel to the coordinate lines ξ_i are calculated at the centers of the control volume faces. The surface area vectors $\mathbf{S}^i$ $(i=1,2,3)$ are also defined at the same points as local contravariant base vectors and are normal to the control volume faces and their magnitude $|\mathbf{S}^i|$ are equal to the corresponding surface areas. V denotes the volume of the control cell.

The quantities $\mathbf{e}_i$, $\mathbf{S}^i$, and V are the basic grid quantities and are directly calculated using discrete grid point coordinates. For convenience of formulation, two additional parameters are defined using the above geometric quantities. The non-orthogonal angles α_i are defined as the angles between the surface area vectors $\mathbf{S}^i$ and the tangential vectors $\mathbf{e}_i$. These angles are a measure of the degree of grid non-orthogonality and are zero for orthogonal grid. The surface area vectors $\mathbf{S}^i$ are re-scaled

DOI: 10.1002/fld

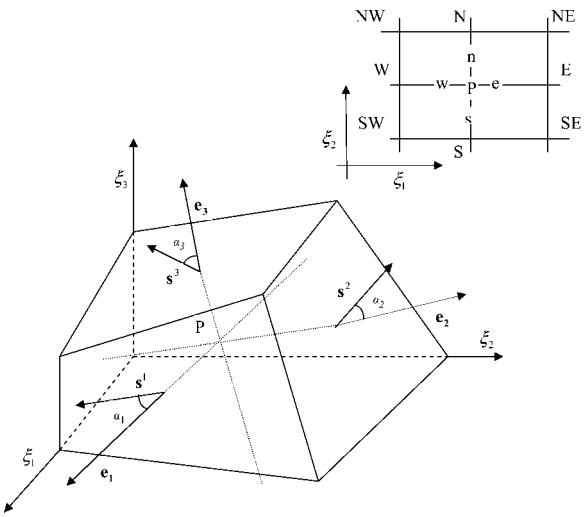

Figure 1. Illustration of the required geometric quantities of a control cell.

and denoted as follows:

$$\mathbf{e}^i = \frac{\mathbf{S}^i}{|\mathbf{S}^i| \cos \alpha_i} \tag{2}$$

which are hereafter called scaled contravariant base vectors. To introduce orthogonal and non-orthogonal terms of metric tensor, consider the steady generalized conservation formulation (1) as follows:

$$\nabla \cdot \mathbf{J} + C = 0 \tag{3}$$

where $\mathbf{J} = \rho \mathbf{u} \phi - \Gamma \nabla \phi$ denotes the total flux. This equation is then integrated over a general control volume shown in Figure 1, as follows:

$$\int_V (\nabla \cdot \mathbf{J} + C)\, \mathrm{d}v = \oint_V \mathbf{J} \cdot \mathrm{d}\mathbf{S} + CV \approx \mathbf{J} \cdot \mathbf{S}^1|_e - \mathbf{J} \cdot \mathbf{S}^1|_w + \mathbf{J} \cdot \mathbf{S}^2|_n$$
$$- \mathbf{J} \cdot \mathbf{S}^2|_s + \mathbf{J} \cdot \mathbf{S}^3|_t - \mathbf{J} \cdot \mathbf{S}^3|_b + CV = 0 \tag{4}$$

The subscripts e, w, n, s, t, and b denote the geographical directions that are used to define neighbor faces (see Figure 1).

Now consider transport of the variable of interest in the ξ_i direction:

$$\mathbf{J} \cdot \mathbf{S}^i = \rho \phi \mathbf{u} \cdot \mathbf{S}^i - \Gamma \nabla \phi \cdot \mathbf{S}^i = \phi F^i - \Gamma \nabla \phi \cdot \mathbf{S}^i, \quad F^i = \rho \mathbf{u} \cdot \mathbf{S}^i \tag{5}$$

Using the definition of gradient operator in curvilinear coordinates,

$$\nabla \phi = \frac{1}{V} \mathbf{S}^i \frac{\partial \phi}{\partial \xi_i} = \frac{1}{V} \left(\mathbf{S}^1 \frac{\partial \phi}{\partial \xi_1} + \mathbf{S}^2 \frac{\partial \phi}{\partial \xi_2} + \mathbf{S}^3 \frac{\partial \phi}{\partial \xi_3} \right) \tag{6}$$

DOI: 10.1002/fld

the following expression for transport of ϕ can be written as:

$$\mathbf{J}\cdot\mathbf{S}^i=\phi F^i-\Gamma g^{ii}\frac{\partial\phi}{\partial\xi_i}-\sum_{i\neq j}\Gamma g^{ij}\frac{\partial\phi}{\partial\xi_j},\quad g^{ij}=\frac{\mathbf{S}^i\cdot\mathbf{S}^j}{V}\quad(i,j=1,2,3)\tag{7}$$

where g^{ij} is the surface area metric tensor. The last term of (7) is a measure of non-orthogonality and is zero for orthogonal grid. Therefore, the total transport of ϕ can be decomposed into orthogonal and non-orthogonal components as follows:

$$\mathbf{J}\cdot\mathbf{S}^i=J_O^i+J_N^i,\quad J_O^i=F^i\phi-\Gamma g^{ii}\frac{\partial\phi}{\partial\xi_i},\quad J_N^i=-\sum_{i\neq j}\Gamma g^{ij}\frac{\partial\phi}{\partial\xi_j}\quad(i=1,2,3)\tag{8}$$

Observe that O and N subscripts refer to orthogonal and non-orthogonal terms, respectively. Substituting Equation (8) into (4), the conservation equation over the control cell can be written as follows:

$$\begin{aligned}&(J_O^1+J_N^1)|_e-(J_O^1+J_N^1)|_w+(J_O^2+J_N^2)|_n-(J_O^2+J_N^2)|_s\\&+(J_O^3+J_N^3)|_t-(J_O^3+J_N^3)|_b+CV=0\end{aligned}\tag{9}$$

The orthogonal component J_O^i has the same form as in the Cartesian coordinate system. It is obvious that the same numerical method as applied in Cartesian coordinates should be used for orthogonal terms. The original method (He and Salcudean [14] method) was used for treatment of the non-orthogonal terms. This method uses the upwinding idea based on geometric properties, see [14] for details, to calculate the non-orthogonal terms that is introduced later in this section. After treating the non-orthogonal diffusion terms in this manner, the general governing equation can be discretized following the standard method developed for Cartesian coordinates as follows:

$$\begin{aligned}a_P\phi_P=&a_E\phi_E+a_W\phi_W+a_N\phi_N+a_S\phi_S+a_T\phi_T+a_B\phi_B+a_{SE}\phi_{SE}+a_{NE}\phi_{NE}+a_{BE}\phi_{BE}\\&+a_{TE}\phi_{TE}+a_{SW}\phi_{SW}+a_{NW}\phi_{NW}+a_{BW}\phi_{SW}+a_{TW}\phi_{TW}\\&+a_{NB}\phi_{NB}+a_{NT}\phi_{NT}+a_{SB}\phi_{SB}+a_{ST}\phi_{ST}+B\end{aligned}\tag{10}$$

where six nearest neighbors of the node 'P' are denoted by E, W, N, S, T, B and corner neighbors are denoted by SE, SW, ST, SB,etc. (see Figure 1) and the source term (B) contains the pressure gradient, body force, and previous time step value. The nearest neighbor coefficients contain both orthogonal (subscripted by 'o') and non-orthogonal (subscripted by 'n') terms (e.g. $a_P=a_{po}+a_{Pn}$). While the orthogonal terms are treated as in Cartesian coordinate system, discretization of non-orthogonal parts of the coefficient are described as follows:

$$\begin{aligned}a_{Pn}=&\tfrac{1}{2}(\Gamma_e(|g_e^{12}|+|g_e^{13}|)+\Gamma_w(|g_w^{12}|+|g_w^{13}|)+\Gamma_n(|g_n^{21}|+|g_n^{23}|)+\Gamma_s(|g_s^{21}|+|g_s^{23}|)\\&+\Gamma_t(|g_t^{31}|+|g_t^{32}|)+\Gamma_b(|g_b^{13}|+|g_b^{23}|))\end{aligned}\tag{11}$$

$$a_{En}=\tfrac{1}{2}(\Gamma_e(|g_e^{12}|+|g_e^{13}|)+\Gamma_n[\![g_n^{21},0]\!]+\Gamma_s[\![-g_s^{21},0]\!]+\Gamma_t[\![g_t^{31},0]\!]+\Gamma_b[\![-g_b^{31},0]\!])\tag{12}$$

Other neighbor coefficients are also calculated similarly. The corner node coefficients (SE, SW, ST, SB, etc.) are obtained after some algebraic manipulation, e.g.

$$a_{SE}=\tfrac{1}{2}(-\Gamma_e[\![g_e^{21},0]\!]-\Gamma_s[\![g_s^{21},0]\!]),\quad a_{NE}=\tfrac{1}{2}(-\Gamma_e[\![-g_e^{21},0]\!]-\Gamma_n[\![-g_s^{21},0]\!])\tag{13}$$

DOI: 10.1002/fld

where $[\![A, B]\!] \equiv \max(A, B)$. The terms containing this operator represent the up-winding scheme based on geometric properties.

Other coefficients can be calculated similarly so that finally we have,

$$a_P = a_E + a_W + a_N + a_S + a_T + a_B + a_{SE} + a_{NE} + a_{BE} + a_{TE} + a_{SW} + a_{NW} + a_{BW} + a_{TW} + a_{NB} + a_{NT} + a_{SB} + a_{ST} + a_P^0 \tag{14}$$

Here a_P^0 denotes the previous time step coefficient.

2.2. Discretization of the NS equations in curvilinear coordinates (the original method)

To discretize momentum equations in a curvilinear coordinate system, different sets of velocity unknowns may be chosen. In this work we adopt physical tangential velocity components (similar to [14]) as dependent variables in momentum and continuity equations. The velocity vector can be expanded in the covariant base vectors as follows:

$$\mathbf{u} = U^{\xi_1}\mathbf{e}_1 + U^{\xi_2}\mathbf{e}_2 + U^{\xi_3}\mathbf{e}_3, \quad U^{\xi_i} = \frac{S^i \cdot \mathbf{u}}{|S^i| \cos\alpha_i} = \mathbf{e}^i \cdot \mathbf{u} \tag{15}$$

A staggered grid arrangement is also used in which the pressure is computed at the geometric center of the control volume and the tangential velocity components U^{ξ_i} are evaluated at the midpoints of the staggered control volume faces.

In order to discretize the momentum equations, auxiliary discretization of the Cartesian velocity components are required. Suppose that all three Cartesian velocity components are computed at the U^{ξ_1}-position. Since the Cartesian velocity components are assumed to share the same control cell as U^{ξ}, the corresponding discretized equations will have identical coefficients. The result can be written in vector form as follows:

$$a_P \mathbf{u}_P = \sum_{nb} a_{nb}\mathbf{u}_{nb} + \sum_{nc} a_{nc}\mathbf{u}_{nc} + B \tag{16}$$

where *nb* represents the six nearest neighbors of the node '*P*', index *nc* represents the corner neighbors as defined previously, and the source term contains the pressure gradient, body force, and previous time step value. To recast the formulation in terms of tangential velocity components as dependent variables, velocity is expanded in the local tangential vector basis at point '*P*'. After taking the inner product of vector $\mathbf{e}_P^1$ and (16) and applying (15), the following equation is obtained:

$$a_P U_P^{\xi_1} = \sum_{nb} a_{nb}(U_{nb}^{\xi_1})' + \sum_{nc} a_{nc}(U_{nc}^{\xi_1})' + S_P^1 \cdot \mathbf{e}_P^1(P_w - P_e) + S_P^2 \cdot \mathbf{e}_P^1(P_s - P_n) + S_P^3 \cdot \mathbf{e}_P^1(P_b - P_t) + \frac{\rho V}{\Delta t}(U_P^{\xi_1})^0, \quad (U_{nb}^{\xi_1})' = \mathbf{e}_P^1 \cdot \mathbf{u}_{nb}, \quad (U_{nc}^{\xi_1})' = \mathbf{e}_P^1 \cdot \mathbf{u}_{nc} \tag{17}$$

The primed velocities $(U_{nb}^{\xi_1})'$ and $(U_{nc}^{\xi_1})'$ are projections of neighboring velocities over the vector $\mathbf{e}^1$ at point '*P*'. The vector $\mathbf{e}^1$ changes from point to point and therefore the velocity $(U_{nb}^{\xi_1})'$ generally

DOI: 10.1002/fld

differs from the actual neighboring variables $U_{nb}^{\xi_1}$. Since the $(U_{nb}^{\xi_1})'$ are not dependent variables, they must be replaced by $U_{nb}^{\xi_1}$ as follows:

$$a_P U_P^{\xi_1} = \sum_{nb} a_{nb} U_{nb}^{\xi_1} + \sum_{nc} a_{nc} U_{nc}^{\xi_1} + S_P^1 \cdot \mathbf{e}_P^1 (P_w - P_e) + S_P^2 \cdot \mathbf{e}_P^1 (P_s - P_n)$$
$$+ S_P^3 \cdot \mathbf{e}_P^1 (P_b - P_t) + \frac{\rho V}{\Delta t} (U_P^{\xi_1})^0 + b^{\xi_1, c} \tag{18}$$

where

$$b^{\xi_1, c} = \sum_{nb} a_{nb} (\mathbf{e}_P^1 - \mathbf{e}_{nb}^1) \cdot \mathbf{u}_{nb} + \sum_{nc} a_{nc} (\mathbf{e}_P^1 - \mathbf{e}_{nc}^1) \cdot \mathbf{u}_{nc} \tag{19}$$

This equation represents the curvature terms when the tangential velocity components are used as velocity unknowns and shows that the curvature terms are produced by the change in vector $\mathbf{e}^1$ from point '*P*' to neighboring points. $\mathbf{u}_{nc}$ and $\mathbf{u}_{nb}$ are calculated using (15) and the discretized equations for the other two velocity unknowns can be derived in a similar manner.

2.3. The modification

First of all, it should be mentioned that for the sake of simplicity the modification is described in 2-D and its extension to 3-D is straightforward. In the original method, described earlier, $\mathbf{u}_{nc}$ and $\mathbf{u}_{nb}$ are calculated using (15) which in 2-D can be expressed as follows:

$$\mathbf{u} = U^{\xi} \mathbf{e}_1 + U^{\eta} \mathbf{e}_2 \tag{20}$$

where U^{ξ} and U^{η} are tangential velocity components in the ξ and η directions. Since these components and also covariant base vectors are known in all grid cells, it is quite straightforward to use them in calculating the curvature terms. Figure 2 shows a schematic smooth grid used to calculate the momentum equation in the η direction. The staggered control volume used to solve this momentum equation has been marked by dashed lines drawn around '*P*'. To compute the curvature terms in curvilinear coordinate, in addition to U^{η} which is known, it is required to calculate U^{ξ} in neighbor points e.g. at the eastern point '*E*'. As shown in Figure 2, U^{ξ} at *E* may be calculated using the neighbor faces with a linear interpolation. This linear interpolation produces satisfactory results for a grid with moderate direction change of the coordinate lines. Now, consider the grid with sharp orientation change in coordinate lines. For the sake of simplicity, suppose that this change occurs only in the ξ direction. Using such grids for complex geometries is usually unavoidable, particularly in 3-D computations. Figure 3 shows a sketch of a grid with discontinuous direction change in ξ coordinate lines.

In order to calculate the momentum equation in the η direction at point *P*, U^{ξ} at neighbor points such as *E* should be computed. At this point U^{ξ} may be determined using its neighbor values by a linear interpolation. These cell faces are shown as an enlarged view in the upper right part of Figure 3. As can be seen from this figure, linear interpolation of the neighbor values would not result in a suitable estimation for U^{ξ} at point *E*. This figure shows that there might be notable difference between true U^{ξ} (aligned in the *ab* direction) and its equivalent $\overline{U}^{\xi}$, resulting from linear interpolation without considering the grid direction changes.

To solve this problem, the direction change effects should be considered in the calculation of tangential velocity components that are used to compute the curvature terms, particularly for grid

DOI: 10.1002/fld

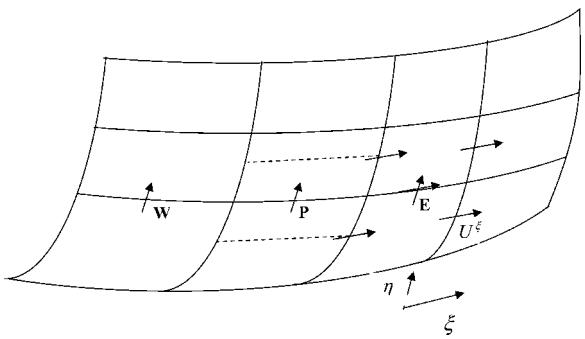

Figure 2. A curvilinear grid with moderate direction change.

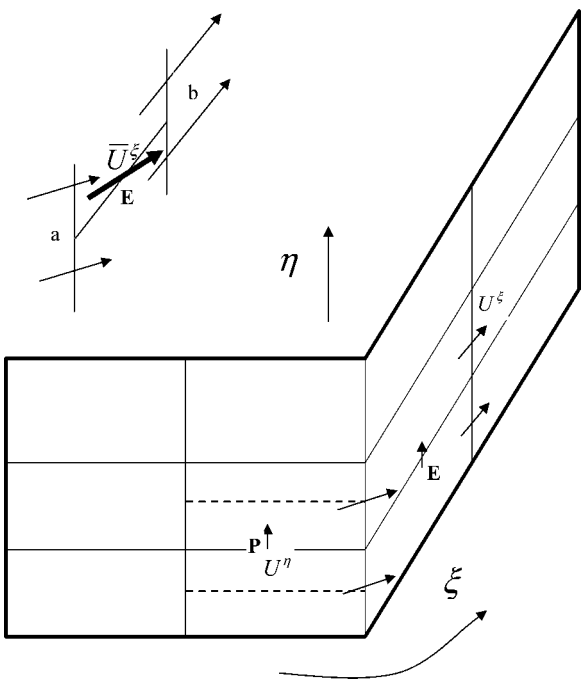

Figure 3. A curvilinear grid with discontinuous direction change.

with rapid changes. Instead of using tangential velocity one may consider the Cartesian velocity components that are independent of grid direction change. Therefore, using Cartesian velocity components obviate the need to consider the grid direction change in the interpolation process. Observe that the Cartesian velocity components were not used in the original method and the present modification consists of using the Cartesian velocity components only for the calculation of curvature terms in momentum equations. Although this strategy seems simple, it brings about large differences in results especially on skewed grids. Figure 4 shows Cartesian velocity components method at point '*E*' that is used for the calculation of curvature terms in Equation (19).

DOI: 10.1002/fld

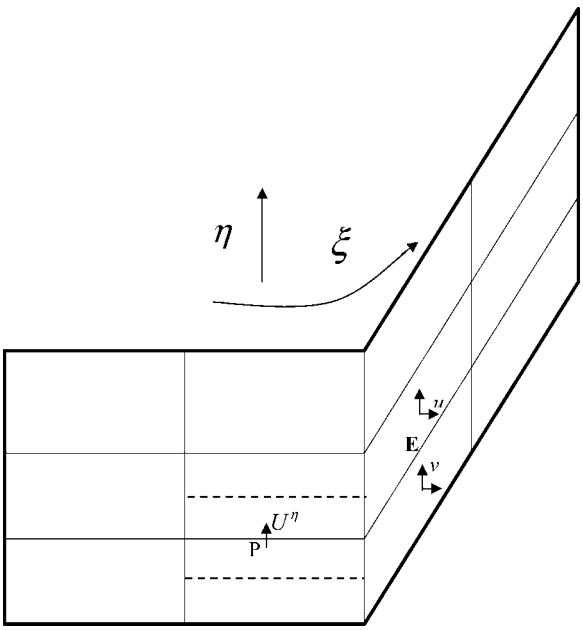

Figure 4. Grid used in modified method for solving equations in the η direction.

2.4. *Discretization of the continuity equation*

Integrating the continuity equation over a control volume shown in Figure 1 and applying the divergence theorem yields:

$$(\mathbf{u}\cdot\mathbf{S}^1)_e-(\mathbf{u}\cdot\mathbf{S}^1)_w+(\mathbf{u}\cdot\mathbf{S}^2)_n-(\mathbf{u}\cdot\mathbf{S}^2)_s+(\mathbf{u}\cdot\mathbf{S}^3)_t-(\mathbf{u}\cdot\mathbf{S}^3)_b\approx\oint_{\Delta v}\mathbf{u}\cdot\mathrm{d}\mathbf{S}=0 \tag{21}$$

Substituting (15) into the above equation yields the discretized equation

$$(c_1U^{\xi 1})_e-(c_1U^{\xi 1})_w+(c_2U^{\xi 2})_n-(c_2U^{\xi 2})_s+(c_3U^{\xi 3})_t-(c_3U^{\xi 3})_b=0,\quad c_i=|S^i|\cos\alpha_i \tag{22}$$

In this formulation the mass conservation equation is expressed exactly in terms of tangential velocity components without any extra source terms. This equation is then used to obtain the pressure correction in the SIMPLE algorithm. Notice that Power-law scheme is used to handle convective terms in momentum equations.

3. RESULTS

In this section few examples are presented to demonstrate the capability of the algorithm to work out various solutions using highly skewed and non-smooth grids. Both 2- and 3-D flow fields are considered. To show the effect of numerical method, it is worthwhile to begin with a careful study of laminar flow that will not be contaminated with turbulence modeling effects and then an assessment of the method in a turbulent regime is made. Notice that all numerical tests are chosen

DOI: 10.1002/fld

in the steady regime. Therefore, Δt in discretized non-dimensionalized NS equations is set equal to infinity in the interest of numerical efficiency. Also notice that the zero body force is used for all these numerical experiments. Test cases are presented using both orthogonal, smooth grids, and skewed non-orthogonal grids and results of the modified method are compared with those of the original one and experiments.

3.1. Flow in a smooth 180° *bend*

Laminar flow with Reynolds number $Re = 50$ (calculated based on duct height and uniform inlet velocity) is solved in a duct with 180° bend. An almost orthogonal 127×27-cell grid is generated. The NS equations in curvilinear coordinates were solved using the original method without any modification. Uniform velocity at the inlet, no-slip boundary condition (BC) at solid walls, and

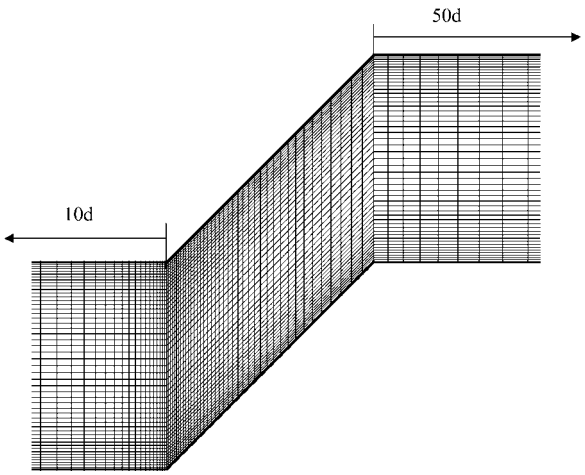

Figure 5. A duct with two 45° sharp bends.

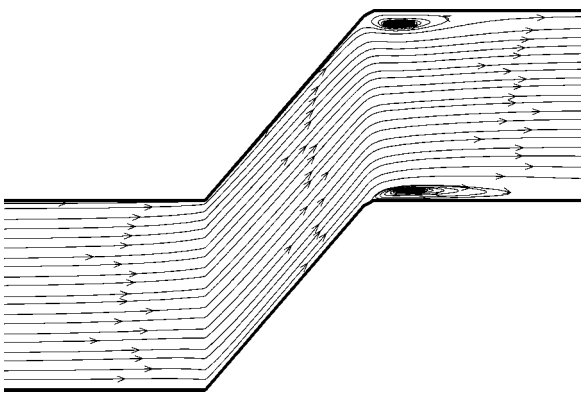

Figure 6. Streamlines from the original method on a non-smooth grid, $Re = 100$, in a duct with two sharp bends.

DOI: 10.1002/fld

fully developed BC at the outlet far from the area of interest were considered. The obtained velocity profile in the fully developed region was parabolic and the maximum velocity was 1.499 times the inlet velocity. This showed that the original method can produce satisfactory results on a smooth curvilinear grid.

3.2. Flow in a duct with two sharp 45° *bends*

In this section, the laminar flow field in a duct with two 45° sharp bends, Figure 5, is computed using uniform velocity at the inlet, fully developed BC at the outlet and no-slip BC at the walls for $Re = 100$ calculated based on duct height and uniform inlet velocity. To reveal the deficiency of the original method, three cases are considered. First, the solution is obtained using the original method on a grid (121×52 cells) with sharp direction changes, then the grid is smoothed and the same method is applied. After that the modified method is implemented using the non-smooth grid.

Figure 6 shows the streamlines in this duct using the original method. The discontinuity of the streamlines near the bends is not physically acceptable. For the second case, the grid is smoothed as illustrated in Figure 7. The streamlines obtained using this grid are depicted in Figure 8. This figure indicates that the streamlines bend more smoothly than the previous case. As can be seen, the solution has been somewhat improved, but the problem has not been solved completely.

The obtained streamlines using the modified method with the first non-smooth grid (Figure 5) are shown in Figure 9. The streamlines are oriented smoothly around the bends in spite of grid line slope discontinuities. The streamline curvature near the corner is much smoother than the former cases. Comparison between Figures 6, 8 and 9 indicates that the separated regions at the corners are strongly affected by the method of solution.

3.3. Development of a 2-D free-stream flow field in a highly non-smooth grid

In this case the superiority of the modification is more clearly shown. The equations of motion are solved with uniform velocity at the inlet, fully developed BC at the outlet, and free-stream BC

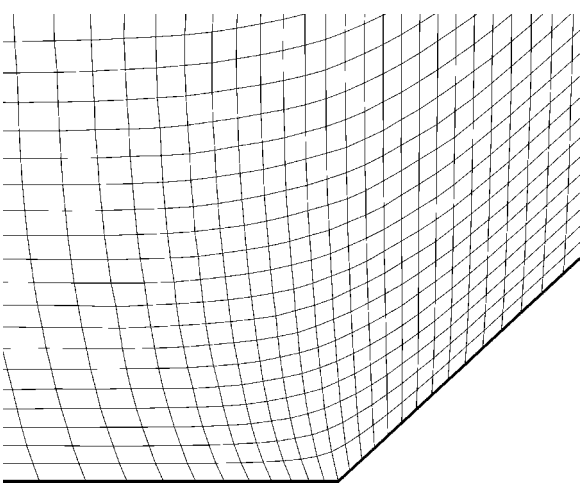

Figure 7. A part of the smooth grid.

DOI: 10.1002/fld

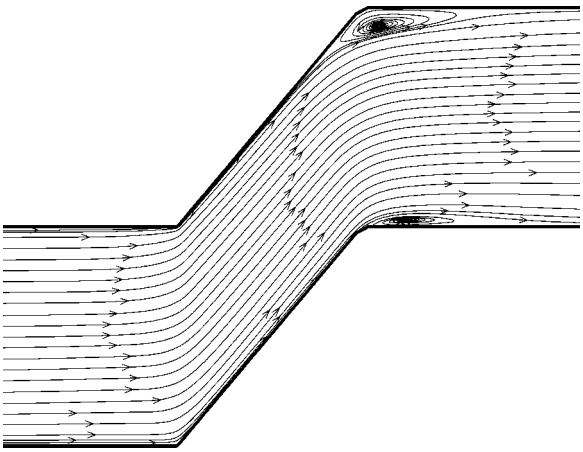

Figure 8. Streamlines from the original method on the smoothed grid, $Re = 100$, in a duct with two sharp bends.

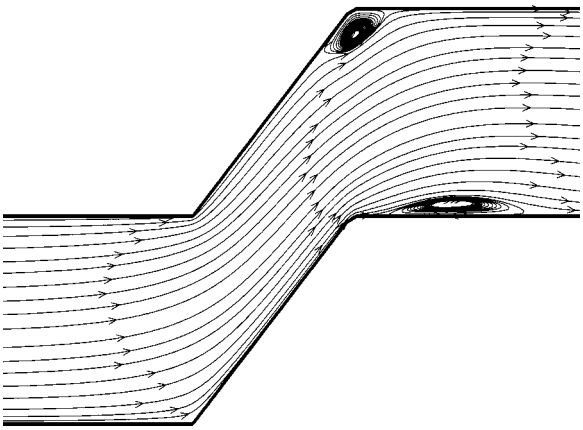

Figure 9. Streamlines from the modified method on the non-smooth grid, $Re = 100$, in a duct with two sharp bends.

on the sides of a very non-smooth grid. The flow is simple but as seen in Figure 10, the grid has been very poorly constructed. The grid skewness is more than 0.7 and the maximum aspect ratio is about 300. Figure 11 displays the streamlines and also vertical velocity component (v) contours. The figure obviously shows the accuracy of the calculation in such a bad grid. It is noteworthy that using this grid, the solution of the original method did not converge at all.

3.4. The flow field about a circular cylinder

This example shows the accuracy of the modified method for a flow field around a solid body. The drag coefficient and the recirculation zone after the object is computed and compared with experimental data [23]. Figure 12 shows the generated grid (192×120 cells) around the cylinder.

DOI: 10.1002/fld

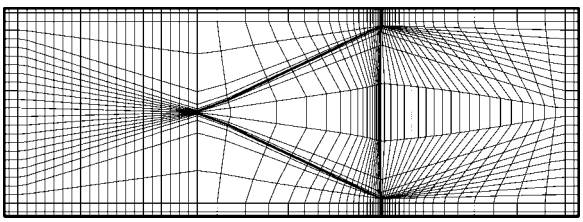

Figure 10. The highly non-smooth grid used for the free-stream flow.

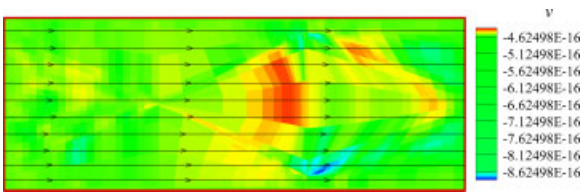

Figure 11. Streamlines and v-velocity contours for the free-stream flow.

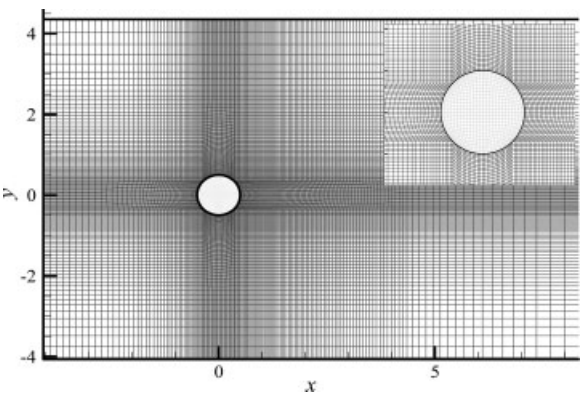

Figure 12. The grid generated around the circular cylinder.

A rapid change in coordinate line direction can be seen adjacent to the object. Inlet velocity BC, fully developed BC at the outlet, and free-stream BC on the sides are used for this steady-state numerical simulation. To keep the flow laminar and steady state, the Reynolds numbers (calculated based on cylinder diameter (D) and U_∞, uniform velocity far from the solid body) are chosen less than one hundred.

Drag coefficients ($C_D = F/\frac{1}{2}\rho U_\infty^2$) and length of recirculation zone versus Reynolds number using two different grid sizes have been shown in Figures 13 and 14, respectively. These clearly show that the modified method is converging to a grid independent solution.

In Figure 15 streamlines and recirculation zone at $Re = 50$ using (a) the modified and (b) the original methods have been compared. The drag coefficient versus Reynolds number obtained using both methods in the coarser grid are plotted in Figure 16. As seen in this figure, drag coefficients

DOI: 10.1002/fld

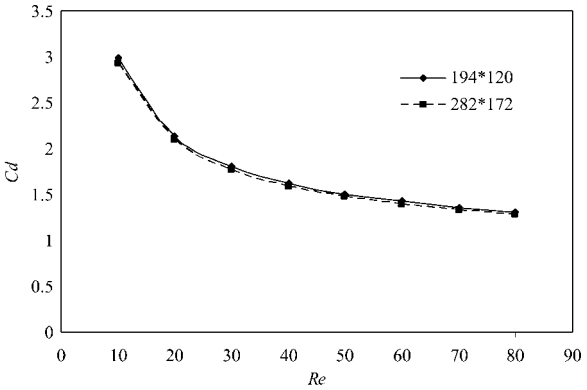

Figure 13. The result of grid study, drag coefficients of the circular cylinder.

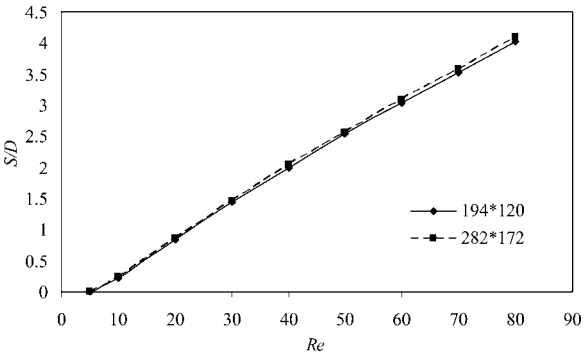

Figure 14. The result of grid study, length of recirculation zone of the circular cylinder.

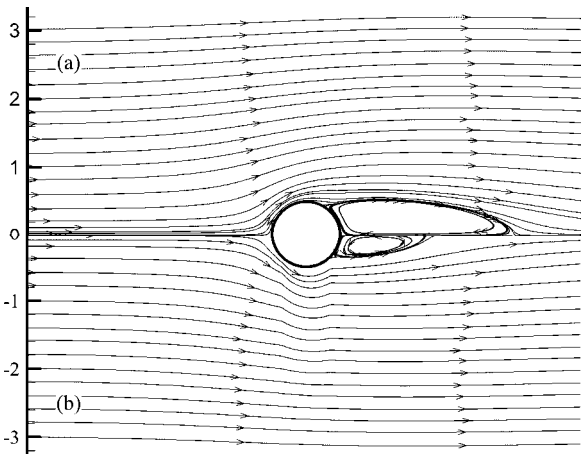

Figure 15. Streamlines about cylinder using modified (a) and original method (b) at $Re = 50$.

DOI: 10.1002/fld

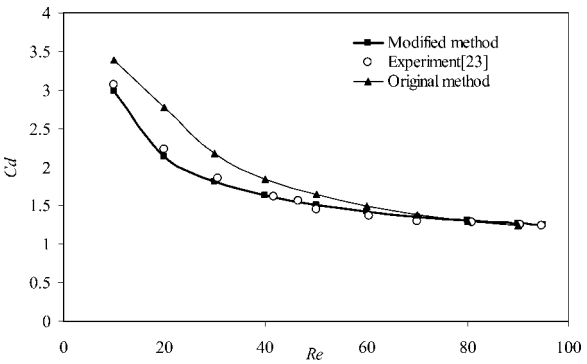

Figure 16. Drag coefficient versus Reynolds number for the flow around a cylinder.

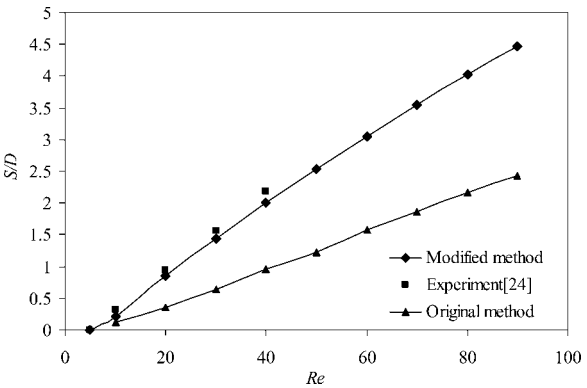

Figure 17. Recirculation zone versus Reynolds number for the flow around a cylinder.

using the original method are larger than experimental data particularly for low Reynolds numbers. Meanwhile this figure shows a good agreement between the solution of the modified method and the experimental data. Figure 17 shows that the recirculation length using the original method is less than experiment (reported by White [24]) and also confirms the superiority of the modified method.

3.5. A 2-D turbulent duct flow

To evaluate the modified method in turbulent regime, a 2-D turbulent duct flow is considered. Here a widely used high-Reynolds number two-equation Reynolds-averaged Navier–Stokes (RANS) model, the standard k–ε method of Launder and Spalding [25] is used to calculate turbulent flow in the duct. The RANS equations are as follows:

$$\frac{\partial(\rho\mathbf{u})}{\partial t}+\nabla\cdot(\rho\mathbf{u}\mathbf{u})=-\nabla p+(\mu+\mu_{\mathrm{T}})\Delta\mathbf{u} \tag{23}$$

$$\nabla\cdot\mathbf{u}=0 \tag{24}$$

DOI: 10.1002/fld

where **u** is now the time-averaged velocity vector $(u, v, w)^{\mathrm{T}}$, ρ is constant fluid density, p is time-averaged pressure, μ is fluid viscosity, and μ_{T} is turbulent eddy viscosity. The eddy viscosity is the only term that must be modeled. In the standard k–ε model, eddy viscosity is calculated as

$$\mu_{\mathrm{T}} = \rho C_{\mu} \frac{k^2}{\varepsilon} \tag{25}$$

where k is the turbulence kinetic energy, ε is the dissipation rate, and C_{μ} is a model constant that must be assigned somewhat arbitrarily. The transport equations for k and ε are:

$$\frac{\partial(\rho k)}{\partial t} + \nabla \cdot (\rho \mathbf{u} k) = \left(\mu + \frac{\mu_{\mathrm{T}}}{\sigma_k}\right) \Delta k + G - \rho\varepsilon \tag{26}$$

$$\frac{\partial(\rho \varepsilon)}{\partial t} + \nabla \cdot (\rho \mathbf{u} \varepsilon) = \left(\mu + \frac{\mu_{\mathrm{T}}}{\sigma_{\varepsilon}}\right) \Delta \varepsilon + C_{\varepsilon 1} \frac{\varepsilon}{k} G - C_{\varepsilon 2} \rho \frac{\varepsilon^2}{k} \tag{27}$$

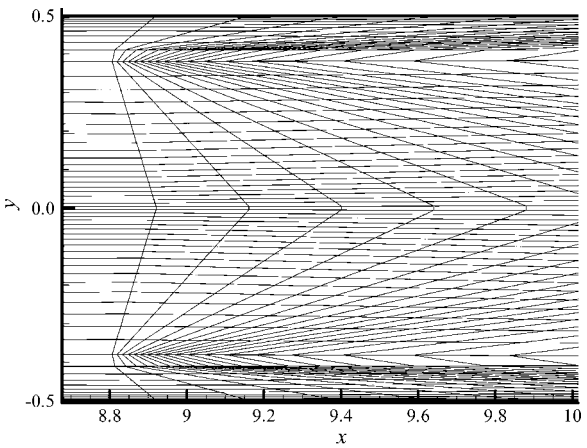

Figure 18. A part of a poorly constructed grid for turbulent flow computation.

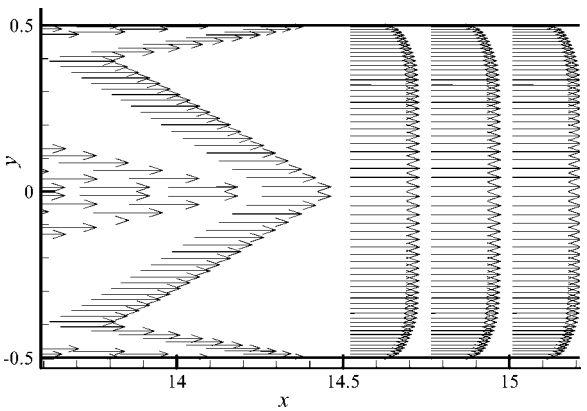

Figure 19. Velocity vectors in a duct with the skewed grid at $Re = 46\,000$.

DOI: 10.1002/fld

where $G=\mu_T(\nabla\mathbf{u}+(\nabla\mathbf{u})^T):\nabla\mathbf{u}$ is the production of turbulence kinetic energy and ':' denotes tensor scalar product. The model closure coefficients employed here are the 'standard' ones (see, e.g. Wilcox [26]): $C_\mu=0.09$, $\sigma_k=1.0$, $\sigma_\varepsilon=1.3$, $C_\varepsilon 1=1.44$, and $C_{\varepsilon 2}=1.92$. The simplified form of the two-layer Chieng and Launder [27] model is adopted to define the wall function for the present study.

The non-dimensionalized RANS equations are discretized using the same approach as employed for laminar flow. All scalar turbulence quantities are evaluated at cell centers. The solution is obtained by the modified method on two different grids, a very poorly constructed 80×60-cell grid, Figure 18, and an appropriate Cartesian grid, while the size of both grids is identical.

A portion of the velocity vectors obtained using the former grid is shown in Figure 19. The velocity profiles using both grids are compared in Figure 20 for $Re=46\,000$ calculated based on duct height (H) and uniform inlet velocity (U). The good agreement between these solutions and Kakac *et al.* [28] numerical results reveals the capability of the modified method to produce satisfactory turbulent result in a really poorly constructed grid where the original one cannot generate even a converged solution in such a distorted grid. Figures 21 and 22 show k and ε profiles in a cross-section at the fully developed region of the duct. It is noteworthy that maximum of k and ε profiles occur near the solid boundary.

3.6. 3-D examples

In this section the modification is extended to the three dimensions and the accuracy of the method is investigated using some test cases.

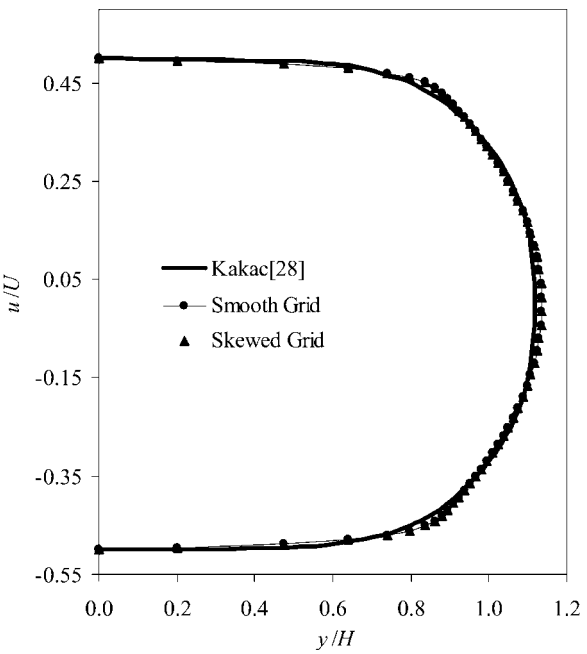

Figure 20. Comparison of u-velocity profile in the fully developed region of the duct.

DOI: 10.1002/fld

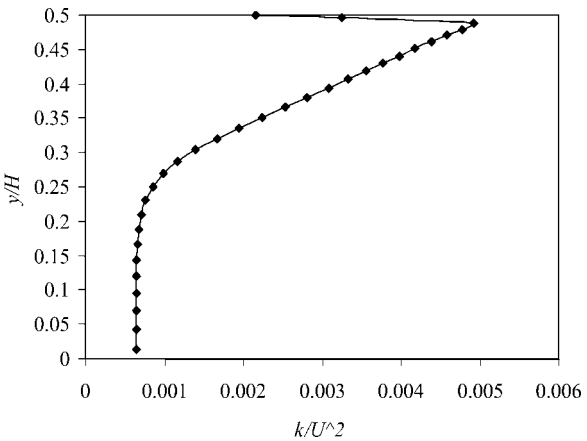

Figure 21. k profile in the fully developed region of the duct at $Re = 46000$.

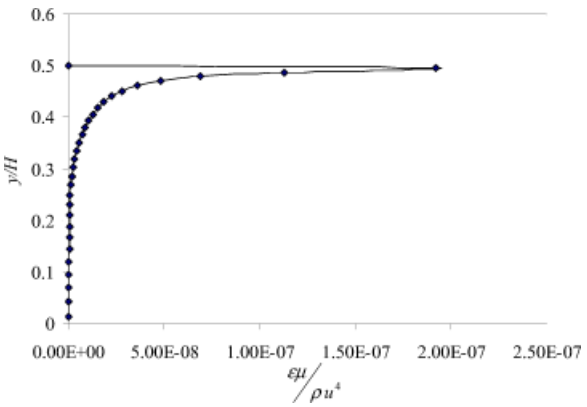

Figure 22. ε profile in the fully developed region of the duct at $Re = 46000$.

3.6.1. Development of a 3-D free-stream flow in a non-smooth grid. A poorly constructed grid similar to the 2-D free-stream flow, Figure 10, was generated for resolving the 3-D NS equations free-stream flow. The obtained streamlines were exactly parallel and velocity components perpendicular to free-stream are almost zero (residual error less than 10^{-10}) which obviously shows the capability of the modified method.

3.6.2. Flow past a sphere. The flow of a viscous fluid past a stationary isolated sphere may be considered as a simplified case of a general family of immersed bluff-body flows with widespread applications. The NS equations are solved using a 66^3-cell grid, illustrated in Figure 23. On the surface of the sphere no-slip BC, homogeneous Neumann BC at the stream wise outlet (x direction) and free-stream BC ($u = 1$, $v = w = 0$) at the transverse outlets (y and z directions) are applied.

In Figure 24 streamlines around the body obtained using (a) the modified and (b) the original method for $Re = 10$ (calculated based on sphere diameter (D) and U_∞, uniform velocity far from

DOI: 10.1002/fld

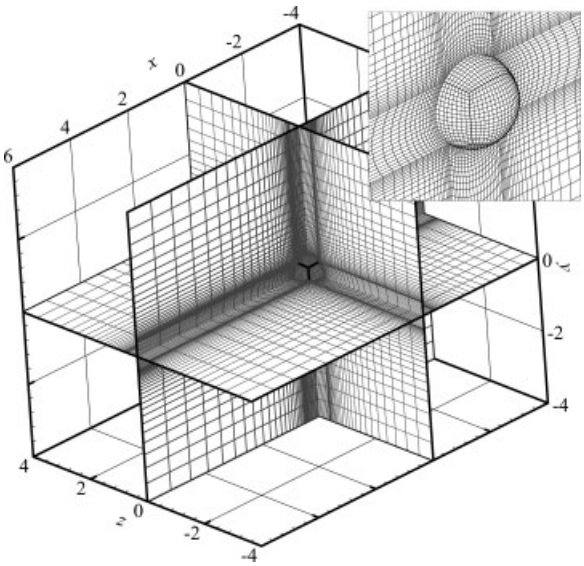

Figure 23. Grids shown on three orthogonal planes through the center of the sphere (left) and an enlarged view on the central plane along the x direction (right).

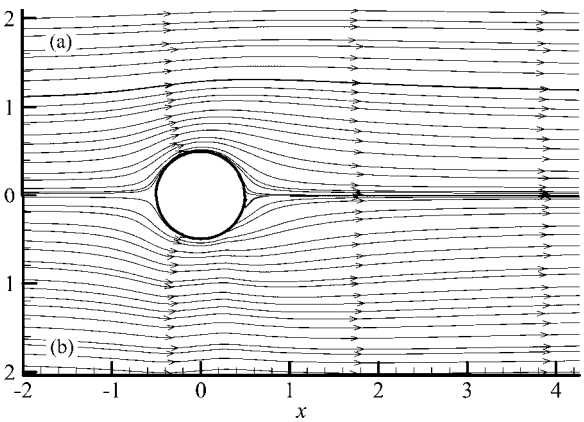

Figure 24. Streamlines of the flow past the sphere obtained from the modified (a) and the original method (b) at $Re = 10$.

the solid body) are compared. As can be seen, streamlines obtained from the modified method, Figure 24(a), are much smoother than the streamlines obtained from the original one, Figure 24(b). These indicate the enhanced accuracy of the modified method solutions on a grid with rapid changes. Further comparison to experimental results can be made with regard to the drag coefficient. There are numerous experimental studies reporting detailed drag coefficient data. However, White [24] presented an empirical formula by curve fitting of the experimental data which is convenient for use. Figure 25 presents computed drag coefficients versus Reynolds number which shows very

DOI: 10.1002/fld

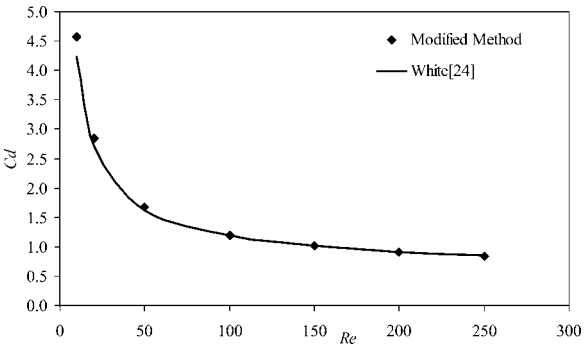

Figure 25. Drag coefficient versus Reynolds number based on the modified method.

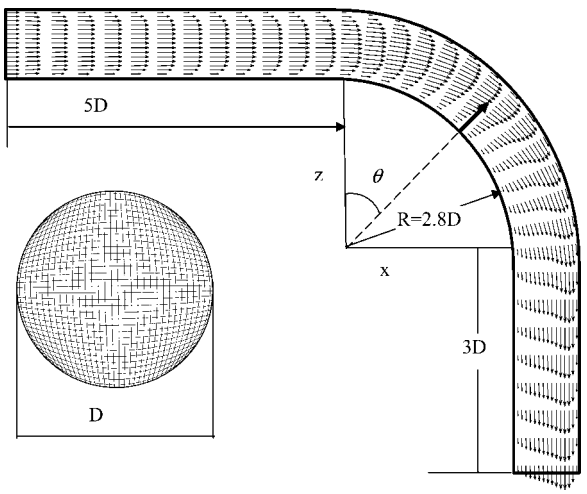

Figure 26. An illustration of geometry and the grid in pipe at $Re = 500$.

good agreement with this empirical formula. It is noteworthy that in this test case the effect of the modification is significant for Reynolds number less than 50 and there are not considerable differences between drag coefficients obtained from these two methods.

CPU times were about a few minutes for 2-D examples and few hours for 3-D test cases on Pentium V processor.

3.6.3. Flow in a pipe with 90° *bend.* For this example, laminar flow in a pipe with 90° bend was considered. Strong secondary flow in this pipe arises from the centrifugal forces due to bend curvature. This flow was studied experimentally by Enayet *et al.* [29]. The geometry and the grid are illustrated in Figure 26. To make the problem tractable using a single PC, a $32 \times 32 \times 74$-cell mesh is chosen for $Re = 500$ calculated based on pipe diameter and inlet uniform velocity. Figure 26 also shows the computed velocity vector in the plane of symmetry. The predicted velocities at one cross-stream ($\theta = 30°$) and the experiment data [29] are plotted in Figure 27. As can be seen,

DOI: 10.1002/fld

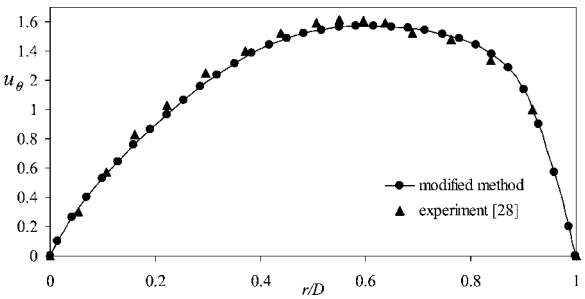

Figure 27. The predicted velocities at one cross-stream ($\theta = 30°$) at $Re = 500$.

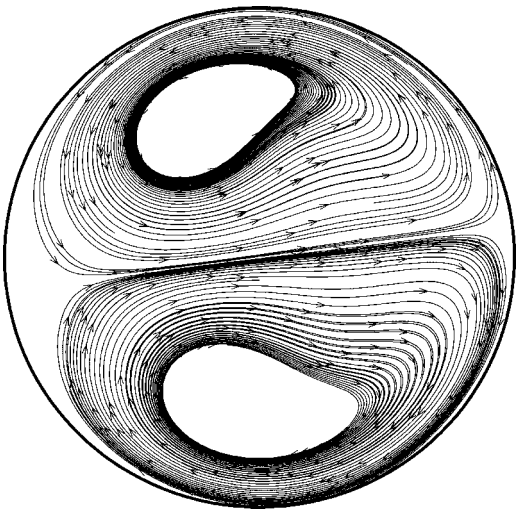

Figure 28. Secondary flow at one cross-stream ($\theta = 75°$) at $Re = 500$.

there is reasonable agreement with the experiment data. Figure 28 displays secondary flow in a cross-section ($\theta = 75°$). It is noteworthy that due to smoothness of the grid, the results of both methods are identical.

4. CONCLUSION

In this paper, a modification of the He and Salcudean [14] approach was proposed to solve NS equations in body conforming grids. This scheme was capable of handling highly non-smooth, non-uniform, and non-orthogonal grids, particularly those having sharp slope discontinuities in the coordinate lines.

The pressure and the physical tangential velocity components were used as dependent variables in momentum equations. The equations were discretized so that various terms such as orthogonal, non-orthogonal, and curvature terms can be easily distinguished. To reduce the sensitivity of the

DOI: 10.1002/fld

curvature terms to rapid change of the coordinate line orientation, the curvature terms were merely computed using Cartesian velocity vectors instead of tangential physical velocities. For precise calculation of these velocity components, the required contravariant base vectors at these points had to be carefully computed.

The method was then applied to solve some fairly complicated 2-D and 3-D flow fields using highly non-smooth grids. The results showed that the modified method was superior to the original method particularly for highly skewed grids.

The result of the modified method for 2-D flow around a cylinder and 3-D flow past a sphere showed good agreement with the experimental data. Using the modified method for free-stream flow in highly skewed 2-D and 3-D grids indicated that this procedure can generate very accurate solution even on such bad grids. The accuracy of the modified method in turbulent regime was also investigated using a highly non-smooth grid in a high-Reynolds 2-D duct flow. Hence, the present method may be an essential part of a 3-D NS robust solver for practical flow configurations.

REFERENCES

1. Thompson JF, Soni BK. *Handbook of Grid Generation*. CRC Press: New York, 1999.
2. Zang Y, Street R, Koseff J. A non-staggered grid, fractional step method for time-dependent incompressible Navier–Stokes equations in curvilinear coordinates. *Journal of Computational Physics* 1994; **114**:18–33.
3. Ikohagi T, Shin B, Daiguji H. Application of an implicit time-marching scheme to a three-dimensional incompressible flow problem in curvilinear coordinate systems. *Journal of Computational Fluids* 1992; **21**: 163–175.
4. Koshizuka S, Oka Y, Kondo S. A staggered differencing technique on boundary-fitted curvilinear grids for incompressible flows along curvilinear or slant walls. *Computational Mechanics* 1990; **7**:123–136.
5. Wesseling P, Segal A, Kassels CGM, Bijl H. Computing flows on general three-dimensional non-smooth staggered grids. *Journal of Engineering Mathematics* 1998; **34**:21–44.
6. Wesseling P, Segal A, Kassels CGM. Computing flows on general three-dimensional non-smooth staggered grids. *Journal of Computational Physics* 1999; **149**:333–362.
7. Lee D, Chiu JJ. Covariant based calculation procedure with non-staggered grid for computation of pulsatile flows. *Numerical Heat Transfer B—Fundamentals* 1992; **1**:269–286.
8. Peric M. Analysis of pressure–velocity coupling on non-orthogonal grid. *Numerical Heat Transfer B—Fundamentals* 1990; **17**:63–82.
9. Edwards MG. M-matrix flux splitting for general full tensor discretization operators on structured and unstructured grids. *Journal of Computational Physics* 2000; **160**:1–28.
10. Graef J, Shivaji R, Soni B, Zhu J. Governing equations of fluid mechanics in physical curvilinear coordinate system. *Differential Equations and Computational Simulations*, *Conference 01*, 1997.
11. Fletcher C. *Computational Techniques for Fluid Dynamics*: *Volume 2*: *Specific Techniques for Different Flow Categories*, 4th Printing (2nd edn). Springer: Berlin, 2000.
12. Lee SL, Chen YF. Non-staggered APPLE Algorithm for incompressible viscous flow in curvilinear coordinates. *Journal of Heat Transfer* 2002; **124**:812–819.
13. Öztop HF. Numerical study of flow and heat transfer in curvilinear ducts: applications of elliptic grid generation. *Applied Mathematics and Computation* 2005; **168**:1449–1460.
14. He P, Salcudean M. A numerical method for 3-D viscous incompressible flows using non-orthogonal grids. *International Journal for Numerical Methods in Fluids* 1994; **18**:449–469.
15. Ziaei AN, McDonough JM, Emdad H, Keshavarzi AR. Using vorticity to define conditions at multiple open boundaries for simulating flow in a simplified vortex settling basin. *International Journal for Numerical Methods in Fluids* 2007; **54**:1–28.
16. Nikseresht AH, Alishahi MM, Emdad H. Complete flow field computation around an ACV (air-cushion vehicle) using 3D VOF with Lagrangian propagation in computational domain. *Computers and Structures* 2008; **86**: 627–641.
17. He P, Salcudean M, Gartshore IS, Nowak P. Multigrid calculation of fluid flows in complex 3-D geometries using curvilinear grids. *Journal of Computational Fluids* 1996; **25**(4):395–419.

DOI: 10.1002/fld

18. Loudyi D, Falconer R, Lin B. Mathematical development and verification of a non-orthogonal finite volume model for groundwater flow applications. *Advances in Water Resources* 2007; **30**(1):29–42.
19. Rüaak W, Rath V, Wolf A, Clauser C. 3D finite volume groundwater and heat transport modeling with non-orthogonal grids, using a coordinate transformation method. *Advances in Water Resources* 2008; **31**(3):513–524.
20. Monaghan JJ, Kos A, Issa N. Fluid generated by impact. *Journal of the Waterway Port Coastal and Ocean Division* (ASCE) 2003; **129**:250–256.
21. Liang G, Sotiropoulos F. A numerical method for solving the 3D unsteady incompressible Navier–Stokes equations in curvilinear domains with complex immersed boundaries. *Journal of Computational Physics* 2007; **225**: 1782–1809.
22. Patankar SV. *Numerical Heat Transfer and Fluid Flow*. Hemisphere Pub.: New York, 1980.
23. Tritton J. Experiments on the flow past a circular cylinder. *Journal of Fluid Mechanics* 1959; **6**:547–567.
24. White FM. *Viscous Fluid Flow* (2nd edn). McGraw-Hill: New York, 1991.
25. Launder BE, Spalding DB. The numerical computation of turbulent flows. *Computer Methods in Applied Mechanics and Engineering* 1974; **3**:269–289.
26. Wilcox DC. *Turbulence Modeling for CFD*. DCW Industries, Inc.: La Canada, CA, 1993.
27. Chieng CC, Launder BE. On the calculation of turbulent heat transport downstream from an abrupt pipe expansion. *Numerical Heat Transfer* 1980; **3**:189–207.
28. Kakac S, Shah RS, Aung W. *Handbook of Single-Phase Convective Heat Transfer*. Wiley: New York, 1987.
29. Enayet MM, Gibson MM, Taylor KP, Yianneskis M. Laser-Doppler measurement flow in a pipe bend. *International Journal of Heat and Fluid Flow* 1982; **3**:213–219.

DOI: 10.1002/fld